Bed slope effects on turbulent wave boundary layers: 1. Model validation and quantification of rough-turbulent results

D. R. Fuhrman,[1] J. Fredsøe,[1] and B. M. Sumer[1]

[1] A numerical model solving incompressible Reynolds-averaged Navier-Stokes equations, combined with a two-equation k-ω turbulence closure, is used to study converging-diverging effects from a sloping bed on turbulent (oscillatory) wave boundary layers. Bed shear stresses from the numerical model are first validated against hydraulically smooth and rough data from flat bed experiments in the form of wave friction factor diagrams. The results show that the model provides acceptable accuracy for wave orbital amplitude to roughness length ratios $a/k_N \geq 20$. Validation against experimental measurements for steady streaming induced by a skewed free stream velocity signal is also provided. We then simulate a series of experiments involving oscillatory flow in a convergent-divergent smooth tunnel, and a good match with respect to bed shear stresses and streaming velocities is achieved. The streaming is conceptually explained using analogies from steady converging and diffuser flows. A parametric study is undertaken to assess both the peak and time-averaged bed shear stresses in converging and diverging half periods under rough-turbulent conditions. The results are presented as friction factor diagrams. A local similarity condition is derived for relating oscillatory flow in a convergent-divergent tunnel, as considered herein, to shoaling shallow-water waves by matching spatial gradients in the free stream orbital length.

1. Introduction

[2] In previous years much effort has been dedicated to the study of various factors capable of promoting net sediment transport rates beneath wave motions. Many of these have focused, for example, on steady streaming effects beneath forward propagating waves [e.g., *Longuet-Higgins*, 1953; *Hedegaard*, 1985; *Justesen*, 1988], as well as effects arising from variations in wave shape (skewness and asymmetry) [e.g., *Ribberink and Al-Salem*, 1994, 1995; *Hassan and Ribberink*, 2005; *Holmedal and Myrhaug*, 2006; *Hsu and Hanes*, 2004; *Gonzalez-Rodriguez and Madsen*, 2007]. These studies have been motivated, at least in part, by the desire to identify and assess various factors believed to play an important role in cross-shore sediment transport, as the understanding of the basic underlying mechanisms involved remains incomplete.

[3] An additional, and potentially important, factor affecting the boundary layer beneath waves propagating normal to beaches, is that of the beach slope itself, which creates a locally converging/diverging flow in successive

wave half cycles. This in turn modifies the pressure gradient within the boundary layer relative to a flat bed, resulting in additional period-averaged bed shear stresses in the onshore direction, as well as additional steady streaming effects. These induced differences in the converging and diverging half cycles are important, as they can potentially create net cross-shore transports of sediment. Additionally, a bottom slope also causes waves to shoal, creating changes in their wave height and wave number in the propagating direction. As will be shown, this particular effect can be considered similar to converging-diverging effects, from the point of view of the wave boundary layer, as both create spatial variations in the free stream velocity characteristics.

[4] Previous work incorporating bed slope effects on the wave boundary layer include the laminar solutions of *Bijker et al.* [1974] for progressive waves and *Blondeaux et al.* [2002] for partially reflected waves on a sloping sea bed. Additionally, *Justesen* [1988] undertook numerical simulations, on the basis of a one-equation turbulence model, for hydraulically rough-turbulent wave boundary layers over sloping sections. However, as no detailed physical experiments involving oscillatory converging-diverging flow were available at that time, the results could not be validated. Such experiments have, however, since been conducted by *Sumer et al.* [1993] who investigated turbulent oscillatory boundary layers within

---

[1]Department of Mechanical Engineering, Technical University of Denmark, Kgs. Lyngby, Denmark.

convergent-divergent channels having smooth walls. More recently, *Zou and Hay* [2003] derived an analytical solution for the turbulent wave boundary layer on a sloping bed, under an assumed (vertically varying, time-constant) eddy viscosity. This solution was then matched to the potential flow theory of *Chu and Mei* [1970] by *Zou et al.* [2003] to give wave orbital velocity predictions for the entire water column.

[5] In this work we will utilize a numerical model solving Reynolds-averaged Navier-Stokes equations, combined with a two-equation (k-ω) turbulence closure, for the simulation of these converging-diverging effects induced by a sloping bed on turbulent wave boundary layers. The motivation is threefold: First, we aim to validate the model against the previous experimental measurements of *Sumer et al.* [1993], which have not been previously simulated. Second, we wish to conduct a parametric study, quantifying the differences in both peak and mean bed shear stresses in the converging/diverging half cycles under rough-turbulent conditions, which should be useful for assessing the sloping bottom effects in practice. Third, we wish to explain precisely how the boundary layer flow in converging-diverging tunnels, as commonly used for physical experiments (and simulated herein), may be related to that beneath real waves in shoaling water, which has not been previously made clear.

[6] The present paper is organized as follows: The numerical model utilized will be briefly described in section 2. The model will be validated against experimental measurements in section 3 for sinusoidal wave motions on both flat and sloping beds, as well as for streaming beneath skewed wave signals. Effects on the maximum and time-averaged bed shear stresses induced by bed slope in the convergent and divergent directions will then be systematically assessed in the form of friction factor diagrams in section 4, for rough-turbulent conditions. A similarity condition for relating the boundary layer beneath converging-diverging oscillatory flow to real-life (shallow-water) waves in shoaling water is derived in section 5. The geophysical relevance of the various results presented is discussed in section 6. Conclusions are finally drawn in section 7.

[7] This paper represents the first of two parts. The second [*Fuhrman et al.*, 2009, hereinafter referred to as Part 2] will present a comparison of the effects of bed slope described above (on bed shear stress parameters and streaming) with those from other factors believed to play a significant role within cross-shore boundary layer processes (e.g., wave skewness, wave asymmetry, conventional steady streaming, and combined wave-current actions (representing, for example, undertow)), with the intent of assessing their likely relative importance.

2. Numerical Model

[8] In this section we will provide a brief description of the computational model used throughout the present work. For brevity, only the equations and boundary conditions are discussed (following *Jakobsen* [2007]), and for details of the (finite volume) numerical schemes employed the interested reader is referred to *Tjerry* [1995] as well as *Tjerry*

and Fredsøe [2005]. The numerical model solves the incompressible Reynolds-averaged Navier-Stokes equations

$$\frac{\partial u_i}{\partial t} + u_j \frac{\partial u_i}{\partial x_j} = -\frac{1}{\rho}\frac{\partial p}{\partial x_i} + \frac{\partial}{\partial x_j}\left[\nu\left(\frac{\partial u_i}{\partial x_j} + \frac{\partial u_j}{\partial x_i}\right) + \frac{\tau_{ij}}{\rho}\right] + F_{Bi}, \quad (1)$$

combined with the local continuity equation

$$\frac{\partial u_i}{\partial x_i} = 0. \quad (2)$$

Here u_i are the mean (phase resolved) velocities, x_i are the Cartesian coordinates, p is the pressure, ν is the fluid kinematic viscosity,

$$\frac{\tau_{ij}}{\rho} = \nu_T\left(\frac{\partial u_i}{\partial x_j} + \frac{\partial u_j}{\partial x_i}\right) - \frac{2}{3}k_T\delta_{ij} \quad (3)$$

is the Reynolds stress tensor, expressing the additional shear stresses due to momentum transfer from turbulent fluctuations, and F_{Bi} represent body forces used to drive the flow, which will be specified in what follows. In (3) δ_{ij} is the Kronecker delta,

$$k_T = \frac{1}{2}\overline{u_i' u_i'} \quad (4)$$

is the turbulent kinetic energy (per unit mass), where the overbar denotes time averaging, and

$$\nu_T = \frac{k_T}{\omega_T} \quad (5)$$

is the eddy viscosity, where ω_T is the specific dissipation rate of the turbulence. To close the system of equations we adopt the two-equation (k-ω) turbulence model of *Wilcox* [1994], utilizing a transport equation for the turbulent kinetic energy

$$\frac{\partial k_T}{\partial t} + u_j\frac{\partial k_T}{\partial x_j} = \frac{\tau_{ij}}{\rho}\frac{\partial u_i}{\partial x_j} - \beta^* k_T\omega_T + \frac{\partial}{\partial x_j}\left[(\nu + \sigma^*\nu_T)\frac{\partial k_T}{\partial x_j}\right], \quad (6)$$

and a transport equation for the specific dissipation rate ω_T

$$\frac{\partial \omega_T}{\partial t} + u_j\frac{\partial \omega_T}{\partial x_j} = \alpha\frac{\omega_T}{k_T}\frac{\tau_{ij}}{\rho}\frac{\partial u_i}{\partial x_j} - \beta\omega_T^2 + \frac{\partial}{\partial x_j}\left[(\nu + \sigma\nu_T)\frac{\partial \omega_T}{\partial x_j}\right], \quad (7)$$

where $\alpha = 5/9$, $\beta = 3/40$, $\beta^* = 9/100$, $\sigma = 1/2$, and $\sigma^* = 1/2$ are standard tuning coefficients.

[9] The above equations are solved in two dimensions, subject to the following boundary conditions. The bottom boundary is considered a friction wall, and no-slip boundary conditions are imposed, i.e., all velocity variables are set to zero, as well as the turbulent kinetic energy k_T. Hence, for hydraulically smooth conditions the bottom boundary may be considered as the location of the smooth wall, whereas for hydraulically rough conditions this may be conceptually taken as near the so-called theoretical wall. The bottom

boundary condition for ω_T is adopted from *Wilcox* [1994], where

$$\omega_T = \frac{U_f^2}{\nu} S_R, \qquad y = 0. \tag{8}$$

The factor S_R is based on the roughness Reynolds number

$$k_N^+ = \frac{k_N U_f}{\nu} \tag{9}$$

where k_N is Nikuradse's equivalent sand grain roughness, and

$$U_f = \sqrt{\frac{\tau_b}{\rho}} \tag{10}$$

is the instantaneous friction velocity, according to

$$S_R = \begin{cases} (50/k_N^+)^2 & \text{for} \quad k_N^+ < 25, \\ 100/k_N^+ & \text{for} \quad k_N^+ \geq 25. \end{cases} \tag{11}$$

This boundary condition has been shown by *Patel and Yoon* [1995] to be valid (on a flat bed) up to at least $k_N^+ = 4000$. A frictionless rigid lid is typically utilized at the top boundary, which is imposed simply as a line of vertical symmetry. The left and right boundaries are connected via periodic conditions. The equations are solved using a PISO algorithm, and the resulting Poisson equation for the pressure is solved with homogeneous Neumann conditions at all boundaries. Within the model computational cells are stretched in the vertical direction to provide adequate resolution of the oscillatory boundary layer. In all cases the model is resolved with 2000 time steps per wave period. We note that the same basic model, but using a k-ϵ turbulence closure, has also been used previously by *Jensen et al.* [1999a, 1999b], *Jensen and Fredsøe* [2001], and *Tjerry and Fredsøe* [2005].

[10] Various types of oscillatory motion will be induced within the model via a forcing term F_B in the horizontal component of (1). The flow is then allowed to develop starting from a motionless initial condition. For the periodic flows considered in the present work, this forcing will generally be of the form

$$F_B = C_B\{U_{1m}\omega\cos(\omega t) + 2U_{2m}\omega\sin(2\omega t)\} + F_{B0}, \tag{12}$$

where U_{1m} and U_{2m} are the desired first and (if necessary) second harmonic free stream velocity amplitudes. Unless stated otherwise, $U_{2m} = 0$. In (12) C_B is a factor which is equal to unity for flat bed cases, where the forcing then simplifies to the desired free stream acceleration $\partial u/\partial t$. It necessarily deviates from unity for cases involving spatial nonuniformity, however, to provide the desired free stream velocity motions. When different from unity the value of C_B used in the model forcing will be reported for completeness. Finally, the F_{B0} term in (12) represents a secondary small global forcing term, which is automatically adjusted internally after each wave period, such that the model tends to a state having negligible net flux (or more generally, any desired flux) in the horizontal direction. This process

typically takes 30–50 wave periods, and results from only the final wave period are analyzed in what follows, where unless otherwise stated $F_{B0} = 0$. Note that this process is necessary even in purely oscillatory flow on flat beds to eliminate spurious effects created from the motionless initial conditions.

3. Model Validation

[11] As a preliminary test of the numerical model, we will first compare results from our simulations against previously made experimental measurements on both flat and sloping beds, in order to establish the model's quantitative accuracy. Particular emphasis will be placed on validating the computed values of the bed shear stress and streaming velocities, as these quantities are of principal interest in the forthcoming sections, as well as in Part 2.

3.1. Validation on Flat Beds

[12] We will first present validation of the numerical model for cases involving oscillatory (sinusoidal) motion on flat (i.e., nonsloping) beds. For the creation of the periodic oscillatory flows used here model forcing is applied as previously described such that the free stream velocity varies sinusoidally, according to

$$u = U_{1m}\sin(\omega t), \tag{13}$$

where U_{1m} is the magnitude of the free stream velocity outside the wave boundary layer. As there is no variation in the (horizontal) x-direction in these cases, the computational domain consists of only 3 cells in the x-direction, the minimum allowed. In the vertical direction 60 computational cells are used, which are stretched to provide adequate resolution of the wave boundary layer. For the present cases we fix $a/D = 1$, where D is the total vertical depth of the flow environment, and

$$a = \frac{U_{1m}}{\omega} \tag{14}$$

is the amplitude of the free stream orbital motion. The parameter a/D is in fact not important on flat beds, provided that the total depth D is large enough not to interfere with the boundary layer. Both hydraulically smooth and hydraulically rough conditions will be considered. For hydraulically smooth cases the nondimensional roughness is fixed to be a large value, $a/k_N = 10^6$. Testing has confirmed that this value is sufficiently large that the computed results become independent of the specified roughness k_N, as should be expected for hydraulically smooth conditions. This can be further confirmed graphically from Figure 2.13 of *Fredsøe and Deigaard* [1992] (adapted from *Justesen* [1988]) utilizing this combination of roughness a/k_N and the range of Reynolds number

$$Re = \frac{aU_{1m}}{\nu} \tag{15}$$

to be considered.
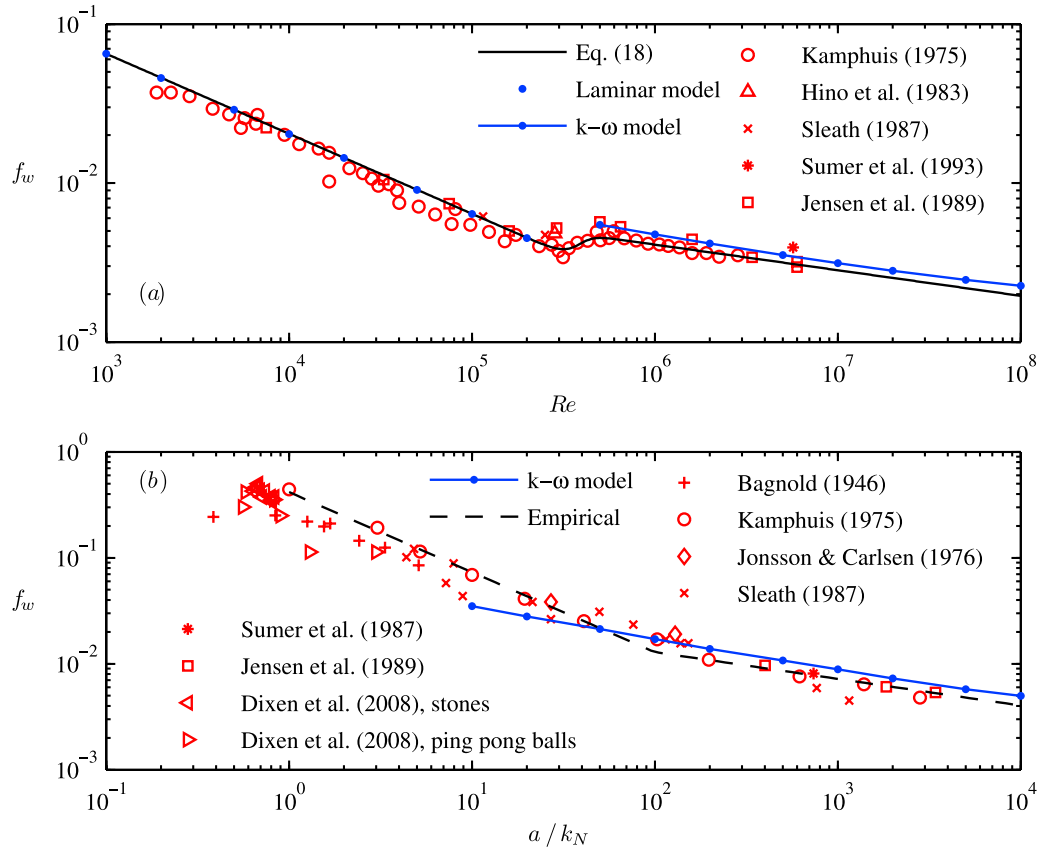
Figure 1. Computed wave friction factor f_w versus (a) Reynolds number Re for hydraulically smooth beds and (b) nondimensional roughness a/k_N for hydraulically rough beds. Numerous experimental data sets are also shown, as well as theoretical/empirical curves for comparison.

[13] Results will be presented in the form of friction factor diagrams, where the wave friction factor f_w is defined according to *Lundgren and Jonsson* [1961]

$$\tau_{bm} = \frac{1}{2}\rho f_w U_{1m}^2, \tag{16}$$

where τ_{bm} is the maximum absolute value of the time varying bed shear stress. Computed results for both hydraulically smooth and rough beds are shown in Figure 1 for the wave boundary layer under the previously described sinusoidal free stream motion. Also shown for comparison are experimental results from *Kamphuis* [1975], *Hino et al.* [1983], *Sleath* [1987], *Jensen et al.* [1989], and *Sumer et al.* [1993]. For hydraulically smooth cases, Figure 1a, both laminar and turbulent cases are shown. The laminar results (i.e., with turbulence model switched off) are seen to match the theoretical variation

$$f_w = \frac{2}{\sqrt{Re}}. \tag{17}$$

The measured smooth turbulent friction factors roughly follow the empirical relationship

$$f_w = 0.037 Re^{-0.16}, \tag{18}$$

which resembles equation (2.55) of *Fredsøe and Deigaard* [1992], but with their factor 0.035 modified slightly to 0.037 to obtain a better match with the experimental values. Notice that (17) and (18) can be combined to give

$$f_w = \frac{2}{\sqrt{Re}} + \frac{1}{2}\left(0.037 Re^{-0.16} - \frac{2}{\sqrt{Re}}\right)$$
$$\cdot \left(1 - \tanh\left[\frac{\pi}{\sqrt{2}} - 1.27 \times 10^{-5}\left(Re - 2 \times 10^5\right)\right]\right), \tag{19}$$

where a hyperbolic tangent function has been used to smoothly connect the laminar and turbulent regimes, giving a reasonable approximation in the transition region as well; This function has been utilized merely for convenience, as it tends to constants (± 1) at positive and negative extremes, while varying smoothly in between. This curve is also shown on Figure 1a for comparison. The computed values in the turbulent regime ($Re > 5 \times 10^5$) match the data reasonably, lying above the empirical curve (18), but seemingly within the span of values experimentally measured by *Kamphuis* [1975], *Jensen et al.* [1989], and *Sumer et al.* [1993] over the range of Re considered. We mention that, using a similar (k-ω^2) turbulence model, *Blondeaux* [1987, Figure 5] computed friction factors that appear to be slightly below those reported here in the smooth-turbulent regime, matching more closely to the data set of *Kamphuis* [1975]. These differences might be

attributed to differences in the ω_T boundary condition, which was not stated explicitly in his paper. We notice that the more recent k-ω model results of *Puleo et al.* [2004, Figure 2a], show overpredicted bed shear stresses relative to wave boundary layer measurements on smooth beds, quite similar to the results presented here. We find the present model results to be sufficiently accurate for our purposes over the range of Reynolds number tested, and we do not consider these discrepancies to be of great concern. Note that, as a check that the present results are sufficiently converged, we mention that doubling the vertical resolution (i.e., using 120 vertical cells) for these smooth wall cases does not modify the results by more than 1%, which is indistinguishable on the scale plotted.

[14] For hydraulically rough conditions, the friction factors become independent of the Reynolds number, but become dependent on the nondimensional roughness a/k_N, as can be seen in Figure 1b. For completeness, however, we note that all computed results shown use fixed $Re = 5 \times 10^6$. In the hydraulically rough regime, the experimental data sets [*Bagnold*, 1946; *Kamphuis*, 1975; *Jonsson and Carlsen*, 1976; *Sleath*, 1987; *Sumer et al.*, 1987; *Jensen et al.*, 1989; *Dixen et al.*, 2008], are seen to reasonably follow

$$f_w = \begin{cases} 0.4\left(\dfrac{a}{k_N}\right)^{-0.75} & \text{for} \quad \dfrac{a}{k_N} < 100, \\ 0.04\left(\dfrac{a}{k_N}\right)^{-0.25} & \text{for} \quad \dfrac{a}{k_N} > 100, \end{cases} \quad (20)$$

where the first expression is from *Fredsøe and Deigaard* [1992, equation (2.43)] and the latter was originally given by *Kamphuis* [1975]. These curves are also shown in Figure 1b for comparison. The model results for $a/k_N > 100$ are seen to fit the experimental data reasonably well, giving slightly larger friction factors than were measured in this range. The model does not capture the qualitative change in the trend of f_w around $a/k_N \approx 10^2$, i.e., very large roughness, where the roughness length becomes a significant fraction of the amplitude of the free stream orbital motion a. This is probably because the model does not capture the flow around individual grains with enough detail [*Fredsøe and Deigaard*, 1992]. Our rough-turbulent results are quite similar to those presented previously by *Blondeaux* [1987], again using a similar turbulence model [see *Blondeaux*, 1987, Figure 8]. From the present comparisons, we deem that the present k-ω turbulence model can be trusted to provide reasonable results and variation with respect to hydraulically rough conditions for say $a/k_N > 20$. Throughout the present work, we will therefore restrict roughness values to be within this range.

3.2. Validation for Skewed Waves

[15] As a second model validation we will compare against measured streaming velocities under a skewed free stream velocity from the experiments of *Ribberink and Al-Salem* [1995]. Similar comparisons have been made previously by *Davies and Li* [1997] and *Holmedal and Myrhaug* [2006]. Streaming is induced under skewed waves due to variations of the turbulence intensity in successive wave half cycles. This gives rise to a period-averaged forcing term in the equation of motion, acting analogously to a

steady horizontal pressure gradient [*Davies and Li*, 1997]. Observed (predominantly negative) streaming under skewed waves near the bed is compensated by positive streaming velocities further up in the water column, ensuring continuity over the vertical section.

[16] *Ribberink and Al-Salem* [1995] considered waves in an oscillating tunnel where the free stream velocity took the form of a second-order Stokes wave

$$u = U_{1m}\sin(\omega t) - U_{2m}\cos(2\omega t). \quad (21)$$

We will consider their case with $U_{1m} = 0.845$ m/s, $U_{2m} = 0.27$ m/s, with angular frequency $\omega = 0.967$ s^{-1}. In their experiments sediment grains with median diameter $d = 0.21$ mm were used. We will simulate this case in two ways. Inspection of their measured period-averaged velocity profile [*Ribberink and Al-Salem*, 1995, Figure 4b] shows that it becomes essentially uniform for $y > 0.15$ m, hence for our first numerical simulation we set the total tunnel depth to be $D = 0.15$ m, where the top boundary corresponds to a frictionless rigid lid. This is convenient in the present context, since the upper boundary conditions ($\partial u/\partial y = 0$, $v = 0$) are essentially satisfied at this location, while their data are also seen to roughly (visually) satisfy continuity over this range (which is not the case further up in the column). Note that this value for D differs from the actual tunnel half-depth 0.55 m, however, thus we are only attempting to match the streaming velocities in the section considered in our comparison. Because of the effective forcing created by the skewed velocity signal, we find that this case requires an eventual global (dimensionless) forcing term of $F_{B0} \cdot D/U_{1m}^2 = 2.10 \times 10^{-4}$ in (12) to ensure continuity over the vertical section. For our second simulation of this case, we will follow closely the methodology of *Davies and Li* [1997], who instead chose to set $D = 0.55$ m, but found that a net flux over the section (and large discrepancies with the data in the upper region) were required to match the streaming near the bed. For our simulation we specify a depth averaged velocity $U/U_{1m} = 0.06$, which we find requires an eventual dimensionless forcing term of $F_{B0} \cdot D/U_{1m}^2 = 2.28 \times 10^{-4}$, i.e., $F_{B0} = 30$ mm/s^2, which is quite close to the 27 mm/s^2 reported by *Davies and Li* [1997]. The above quantities lead to the nondimensional parameters $Re = 7.39 \times 10^5$, $a/k_N = 1.67 \times 10^3$, $a/D = 5.83/1.59$ (first/second simulation), and $U_{2m}/U_{1m} = 0.32$, where $k_N = 2.5d$ has been assumed. Thus, this case represents hydraulically rough-turbulent conditions. For both simulations we use a nonsloping bed, with 60 points in the vertical direction, stretched to properly resolve the bottom boundary layer in each case.

[17] Comparison of the measured and computed streaming velocities are provided in Figure 2, for both simulations. For the first case ($D = 0.15$ m (Figure 2a)), a reasonable match is observed with the data in the modeled section ($y/D < 1$) near the bed. The measurements further up in the physical tunnel are also shown for completeness, which are seen to be roughly uniform, as described above. The results using the second methodology ($D = 0.55$ m) are similarly provided in Figure 2b. A similar match is observed in the near-bed streaming region, with the previously stated large discrepancies with the data apparent in the upper fluid region. The result depicted in Figure 2b is quite similar to
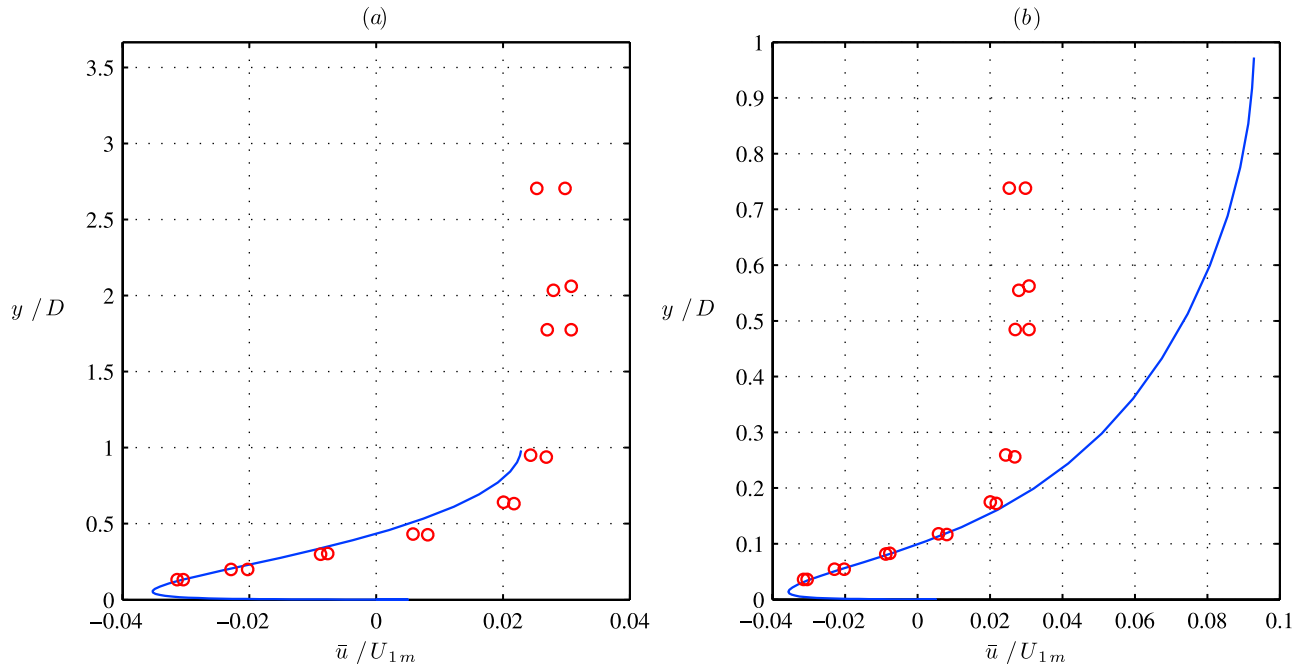
Figure 2. Comparison of computed (full line) and measured (circles) [*Ribberink and Al-Salem*, 1995] horizontal velocities under a skewed free stream velocity signal with (a) $D = 0.15$ m and zero net flux and (b) $D = 0.55$ m with depth-integrated current $U/U_{1m} = 0.06$.

that achieved previously by *Davies and Li* [1997] using their similar methodology (compare with *Davies and Li* [1997, Figure 6(ii)]. Hence, this simulation can be considered as an independent repetition of their findings. On the basis of these comparisons, we find that these results sufficiently validate the model for rough-turbulent streaming under skewed free stream velocity signals. Note also that the demonstrated accurate streaming near the bed for this case implies accurate period-averaged shear stresses within the same section of fluid.

[18] Although we will not specifically consider skewness effects further in the present paper (Part 1), this validation is relevant as wave shape effects will be thoroughly considered in Part 2.

3.3. Validation on Sloping Beds

[19] Having systematically assessed the model accuracy for computing bed shear stresses on flat (nonsloping) beds, we will now turn our attention to similar simulations involving sloping beds, which is the primary focus of the present work. Specifically, we will compare simulated results against the experimental measurements of *Sumer et al.* [1993], who measured bed shear stresses, period-averaged velocity profiles, and turbulence characteristics for oscillatory flow in a smooth convergent-divergent tunnel. To the authors' knowledge, the present work represents the first numerical comparison against this particular data set.

[20] In their experiments, *Sumer et al.* [1993] created converging-diverging sections by mounting sloping sections on the top of a "u-tube" oscillating tunnel facility. *Sumer et al.* [1993] considered two such sections, having $\beta \approx 0.5°$ and $\beta \approx 1°$, where 2β is defined as the angle formed by the sloping section and the horizontal upper lid. Our numerical representations of these two cases are provided in Figure 3,

which can be seen to closely resemble the experimental configurations described by *Sumer et al.* [1993] in a nondimensional sense, [see *Sumer et al.*, 1993, Figure 1]. (Note that the vertical scale in Figure 3 is grossly exaggerated.) To match the experimental conditions, no-slip walls are placed at both top and bottom boundaries. Both model setups utilize a 120×100 computational grid, which is stretched in the vertical direction, with cells clustered at both the top and bottom boundaries in order to adequately resolve both boundary layers. As can be seen from the axes on Figures 3a and 3b, we use the normalizing length D, which here corresponds to the centerline depth (i.e., half the total tunnel depth) at the origin $x/D = 0$, which is placed in the middle of the sloping section. Hence, in the present context, the physically relevant slope is that of the tunnel centerline $s = \tan \beta$, as this may be taken (roughly) as a line of vertical symmetry. Periodic forcing is applied to the model as before to create a sinusoidal free stream motion at each section, though because of the sloping section the amplitude of this motion now varies with x. Unless otherwise noted, the variable U_{1m} will specifically refer to the magnitude of the oscillatory free stream velocity (here taken at the tunnel centerline) at $x/D = 0$, however. To give the desired free stream motions, we mention for completeness that the cases with $\beta \approx 0.5°$ use a model forcing factor in (12) of $C_B = 0.83$, whereas those with $\beta \approx 1°$ use $C_B = 0.88$. As the experiments were made with smooth walls, we set the nondimensional roughness $a/k_N = 10^6$, as before.

[21] We will here focus on the bed shear stress and period-averaged velocity profile measurements of *Sumer et al.* [1993] for further validation purposes. Specifically, we will (primarily) utilize results from their test cases 1, 3, and 7 for bed shear stress values on various tunnel slopes; and from their tests 14−17 for streaming induced by the
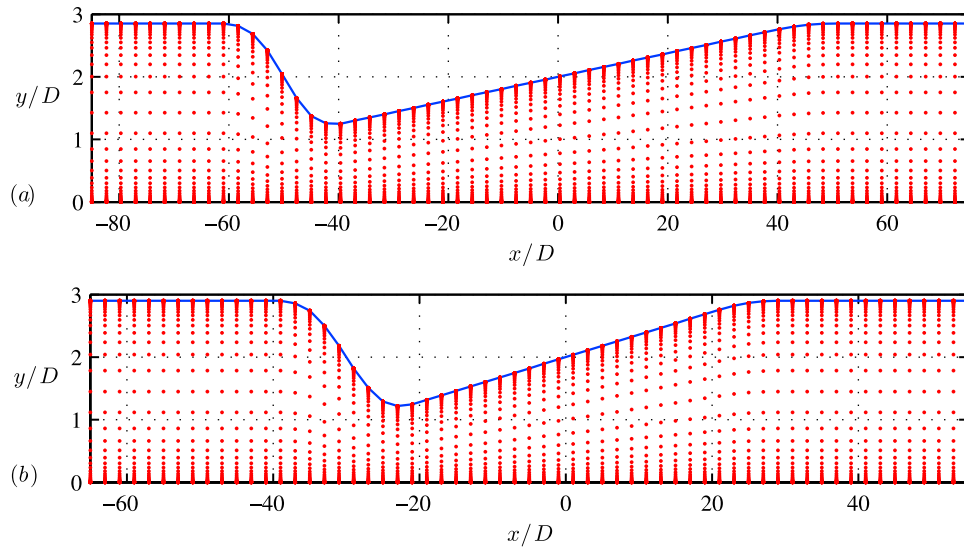
Figure 3. Computational grids used for the sloping bed experiments with (a) $2\beta = 1.082°$ and (b) $2\beta = 2.062°$, where 2β is the angle between the sloping section and the horizontal. Note the different horizontal scales and grossly exaggerated vertical scales on Figures 3a and 3b.

converging-diverging flow. We note that their test 1 corresponds to an oscillatory flow in the u-tube in the absence of either sloping section, serving as a flat bed reference, while tests 14–17 in fact consist of a single physical setup, with velocity measurements taken at four separate cross sections. A summary of nondimensional quantities for the various test cases considered is provided in Table 1, with the reported values referring to the quantities at the middle of the sloping region, i.e., at the origin $x/D = 0$. For later comparison, we also tabulate values of the quantity sa/D in Table 1. This represents a similarity parameter, the importance of which will be clarified in section 5.

[22] Comparison of the computed and measured time series for the free stream velocity and bed shear stress for test 1 ($\beta = 0°$), test 3 ($\beta \approx 0.5°$), and test 7 ($\beta \approx 1°$) are provided in Figure 4. Generally, the normalized free stream velocities in the model match those from the experiments quite well, as indicated on Figures 4a, 4b, and 4c, confirming that the driving free stream motion has been adequately reproduced within the numerical model. The time series of computed bed shear stresses (Figures 4d, 4e, and 4f), however, seem to be somewhat under-predicted, by roughly 20% at the peaks, when compared against the measured values. Regarding this issue, we return attention back to Figure 1a, where the measured result (corresponding to the flat bed case, i.e., test 1) for the maximum bed shear stress, in the form of the friction factor, is shown by the lone asterisk. As can be seen, these particular measurements are somewhat above the other data in this regime from *Jensen et al.* [1989]. Hence, while the present agreement (Figure 4) is not perfect, the results would appear to be within the (visual) scatter from the available experiments for this range of the Reynolds number, i.e., the present model results (for the maximum bed shear stress) lie in between the reported measurements of *Jensen et al.* [1989] and *Sumer et al.* [1993] for $Re \approx 5 \times 10^6$. Qualitatively, we also notice important similarities between the computed and measured bed shear stress time series. Most notably, both show a

larger bed shear stress in the converging (negative) direction than in the diverging (positive) direction.

[23] As an additional check, a comparison of the computed and measured period-averaged bed shear stress for these three cases is provided in Figure 5. Also shown for comparison are the measured experimental results for additional cases with slightly varying a/D values, taken from *Sumer et al.* [1993, Figure 5]. As can be seen, in both measurements and the numerical simulations, a period-averaged bed shear stress in the direction of convergence is predicted. In terms of these period-averaged bed shear stresses, a good quantitative match with the measured data is achieved, as seen in Figure 5. Hence, while the instantaneous values of bed shear stress are somewhat under-predicted relative to the reported measurements, the period-averaged values in the direction of convergence seem to be in good agreement, implying an apparent cancelation of the bed shear stresses in the over/under predicted peak/trough regions.

[24] The presence of period-averaged bed shear stresses can be qualitatively explained by the fact that the converging-diverging nature of the flow will result in decreasing pressures in the convergent direction (velocity magnitudes will increase in the converging direction, hence pressures will decrease). Outside the boundary layer potential flow may reasonably be assumed, and the pressure gradient will be balanced by convective momentum. Inside the boundary

Table 1. Summary of Nondimensional Parameters Used in the Oscillating Tunnel Experiments of *Sumer et al.* [1993][a]

Test	Re	a/D	β (deg)	sa/D
1	5.7×10^6	20	0	0
3	6.2×10^6	30	0.541	0.28
7	5.9×10^6	29.5	1.031	0.53
14–17	6.0×10^6	31	1.031	0.56

[a]All reported values correspond to those at the middle of the sloping section $x/D = 0$.
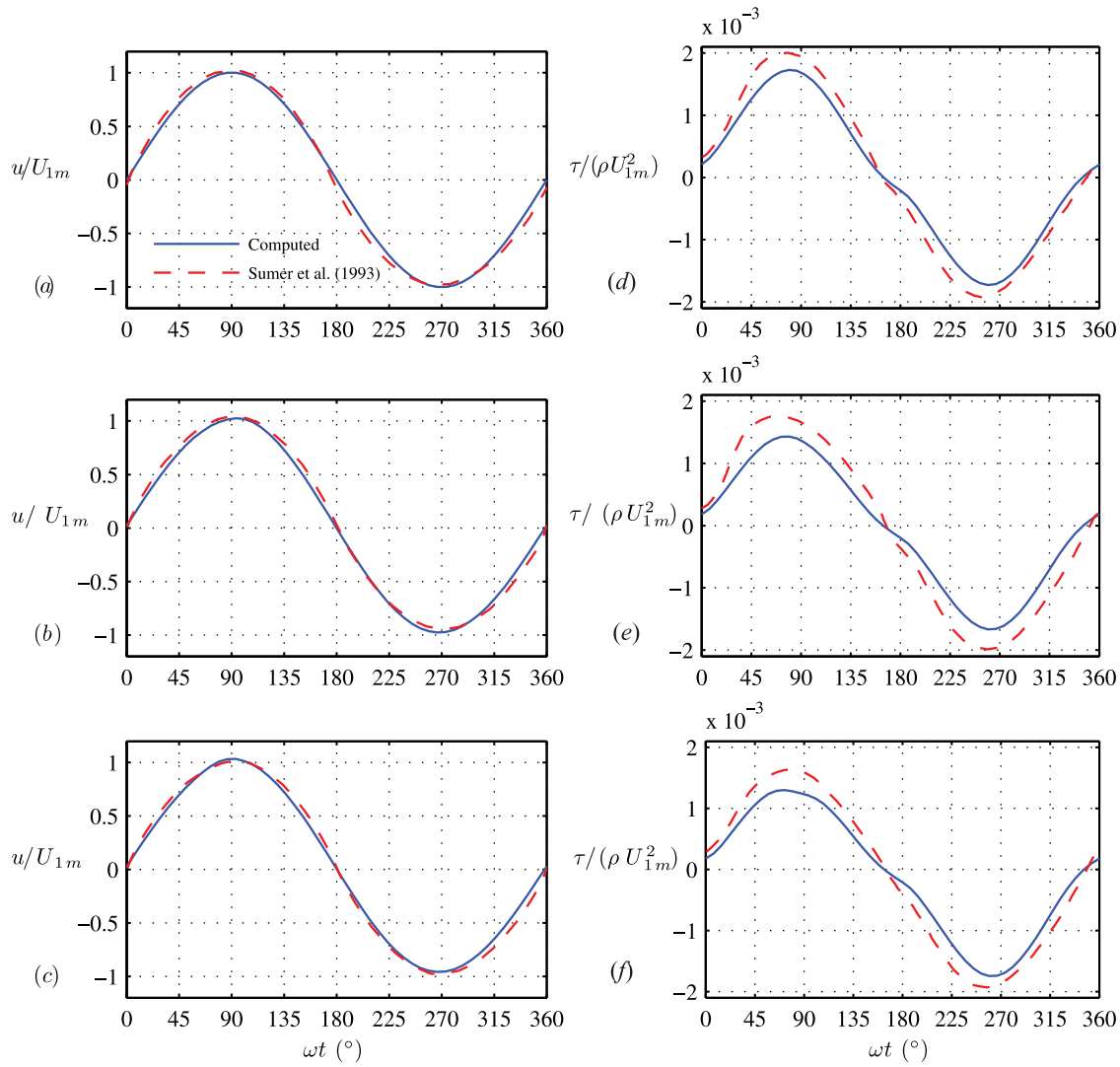
Figure 4. Comparison of computed (full lines) and measured (dashed lines) (a, b, c) free stream velocity and (d, e, f) bed shear stress for test 1 with $\beta = 0°$ (Figures 4a and 4d), test 3 with $\beta = 0.541°$ (Figures 4b and 4e), and test 7 with $\beta = 1.031°$ (Figure 4c and 4f). All results correspond to $x/D = 0$, with free stream velocities taken at $y/D = 1$.

layer, however, the pressure gradient will be practically unchanged (assuming small boundary layer thickness), whereas the velocities (and thereby the convective momentum) will become smaller. Hence, additional period-averaged shear stresses must develop to maintain a force balance. Near the bed the period-averaged shear stress on the fluid must oppose that from the pressure gradient, corresponding to the observed bed shear stresses in the convergent direction.

[25] The nonzero period-averaged bed shear stresses induced by the sloping section will in turn drive period-averaged circulation currents, which we will refer to as additional streaming. Because the period-averaged fluid shear stress is, to leading-order, related to the gradient of the period-averaged horizontal velocity by

$$\frac{\bar{\tau}}{\rho} = \overline{(\nu + \nu_T)\frac{\partial u}{\partial y}}, \qquad (22)$$

which stems from (3), while also adding the viscous component from (1), it follows that (usually)

$$\frac{\bar{\tau}}{\rho} \propto \frac{\partial \bar{u}}{\partial y}, \qquad (23)$$

since both ν and ν_T are always positive. (An exception to this rule of thumb occurs, for example, in the streaming under skewed and asymmetric waves, as will be shown in Part 2.) Thus, streaming in the direction of convergence should be expected near the bed.

[26] Near-bed streaming in the direction of convergence can alternatively be explained via the boundary layer response to favorable (adverse) pressure gradients in the converging (diverging) half cycles. The velocity profiles under these two conditions are demonstrated conceptually for steady flow conditions in Figure 6. As shown, the profile under a diverging (diffuser) flow (Figure 6a) significantly reduces the velocity gradients (and hence, the velocities)
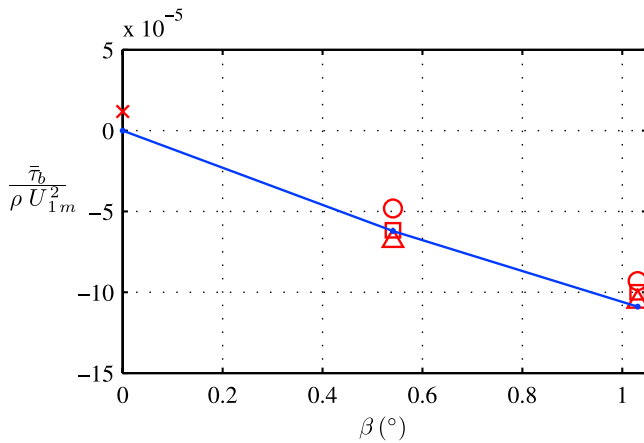
Figure 5. Comparison of computed (full line) and measured (symbols) period-averaged bed shear stress values from *Sumer et al.* [1993] versus β, where the measurements correspond to test 1 with $a/D = 20$ (multiplication signs), cases with $a/D = 27$ (circles), tests 3 and 7 with $a/D \approx 30$ (triangles), and cases with $a/D = 34$ (squares).

near the bed, whereas a converging flow (Figure 6b) takes a form similar to that of an ordinary boundary layer. The period-averaged streaming profile under oscillatory flow conditions can then be taken conceptually as the average of these two scenarios. Clearly, the flow near the bed in the converging case exceeds that from the diverging case, whereby near-bed streaming in the convergent direction should be expected. This will in turn be compensated by a period-averaged flow in the opposite (divergent) direction further up in the water column, such that there is no net flux over each vertical section. A conceptual sketch of the resulting circulation currents is provided in Figure 7.

[27] As a final comparison against the data set of *Sumer et al.* [1993], we consider model results for the streaming on the basis of their tests 14–17. As mentioned previously, these four cases in fact come from a single simulation, with
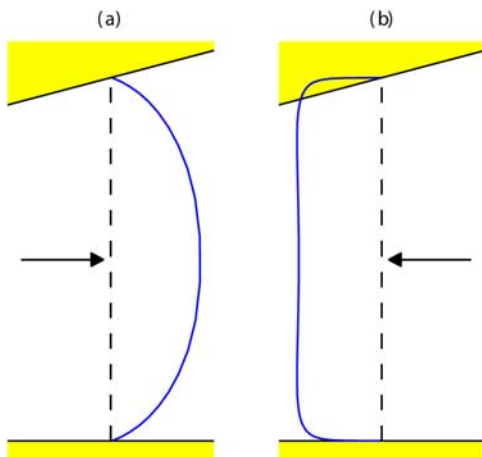

Figure 6. Conceptual sketch showing the velocity profile in (a) a diverging (diffuser) flow, where the pressure gradient is adverse, and (b) a converging (boundary layer) flow, where the pressure gradient is favorable. The arrows indicate the direction of flow.
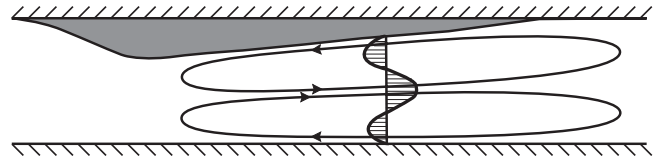

Figure 7. Conceptual sketch of the recirculating flow system induced by the convergent-divergent geometry of the tunnel.

the various profiles corresponding to various x/D values depicted in Figure 3b. As a first demonstration, horizontal velocity profiles averaged over the converging and diverging half periods (at the middle of the slope, $x = 0$) are presented in Figure 8. To ease comparison, both profiles are presented as positive on Figure 8. These are clearly seen to resemble the conceptual sketches shown previously in Figure 6 for these two conditions, seemingly confirming the above conceptual explanation of the near-bed streaming.

[28] The velocity profiles averaged over the full period are shown for the four measurement locations in Figure 9. Note that Figure 9b represents the average of the two profiles shown in Figure 8, after accounting for a sign reversal for the converging half-period results. As expected, a period-averaged near-bed flow in the direction of convergence is indeed produced in both the experiments and simulations, whereas it is in the opposite direction further away from the walls. As can be seen in Figure 9, the model results are generally in good agreement with the measurements at all four cross sections, though it is stressed that there is a lack of experimental data in some of the near-wall regions (especially, for example, near the top walls in Figures 9c and 9d). The most noticeable discrepancy is the apparent slight up-shifting of the measurement data relative to the simulations. This is apparent in Figures 9b
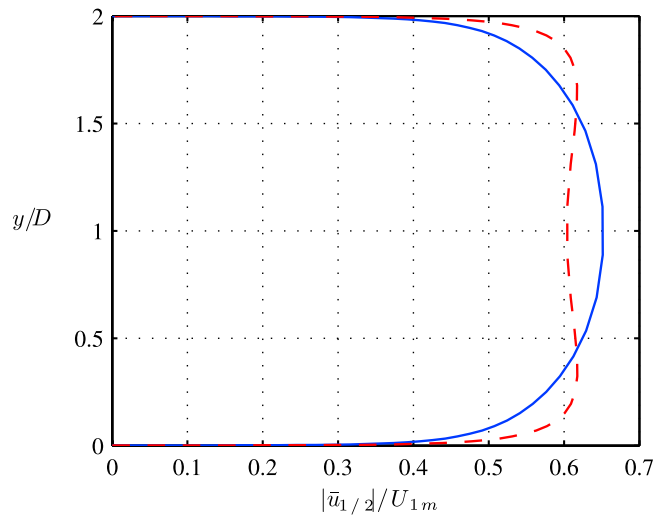
Figure 8. Computed (absolute values) for the horizontal velocity profile averaged over the diverging half period (full line) and converging half period (dashed line) at $x/D = 0$ from test cases 14–17 of *Sumer et al.* [1993]. The full period-averaged velocity profile for this location is given in Figure 9b.
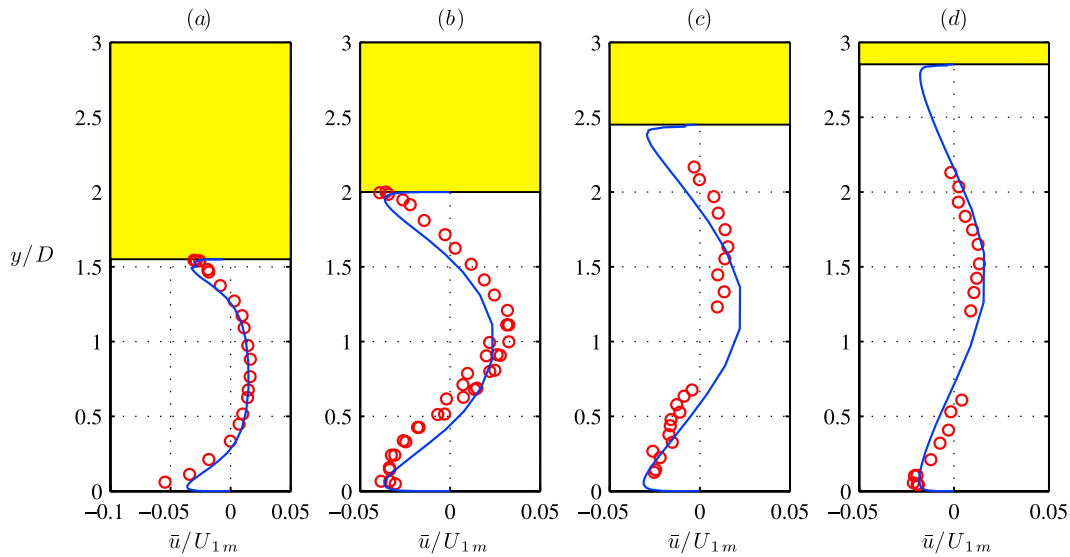
Figure 9. Computed (full line) and measured (circles) period-averaged velocity profiles for test cases 14–17 of *Sumer et al.* [1993], with $Re \approx 6.0 \times 10^6$ at (a) $x/D = -12.5$, (b) $x/D = 0$, (c) $x/D = 12.5$, and (d) $x/D = 24.5$.

and 9c, but not so apparent in Figure 9a and 9d. Generally, we find the present comparison for the streaming for the entire profile to be acceptable. This demonstrates acceptable accuracy of the numerical model for the quantities of principal interest (bed shear stresses and streaming velocities) induced by converging-diverging bed slope effects.

4. Rough-Turbulent Results

[29] With the model sufficiently validated against available physical experiments involving oscillatory convergent-divergent flow on smooth beds (section 3.3), it will now be used to systematically study the convergent-divergent effects induced by a bottom slope under hydraulically rough-turbulent conditions, the situation most likely encountered in practice. Emphasis will be placed on the behavior of the bed shear stress in the convergent and divergent half periods, as these are of principle interest, for example, in potentially creating net transports of sediment over full wave cycles.

4.1. Model Setup

[30] Our model setup now consists of a symmetric domain containing regions of positive and negative slope connected by a flat section, an example of which is shown

in Figure 10. (Note again that in Figure 10 the vertical scale is grossly exaggerated.) Model forcing is applied as before, to create an oscillating (sinusoidal) free stream velocity according to (13) at each vertical section. Spatially periodic boundary conditions are again utilized to connect the left and right boundaries. A no-slip wall is placed along the bottom, whereas the top boundary now corresponds to a frictionless rigid lid. This is advantageous to the setup in section 3.3 (where no-slip walls were used at both top and bottom boundaries), since only the bottom boundary layer develops and needs to be resolved. All length scales are again normalized by a quantity D, which is now defined as the total height of the numerical flume at the middle of the left sloping section, which is taken as the origin $x/D = 0$, see again Figure 10. For a given tunnel slope $s = \tan \beta$, where β defines the slope angle, the total length of the sloping sections is set to be $L_s = D/s$. This creates a total tunnel height ranging from $3D/2$ at its deepest location to $D/2$ at its most constricted location. A forcing factor $C_B = 1.17$ in (12) has been found to provide the desired free stream velocity signal for these configurations. All simulations use a 120×60 cell mesh, stretched in the vertical direction (see Figure 10) to adequately resolve the bottom boundary layer. All reported results will be taken from the cross section at $x/$
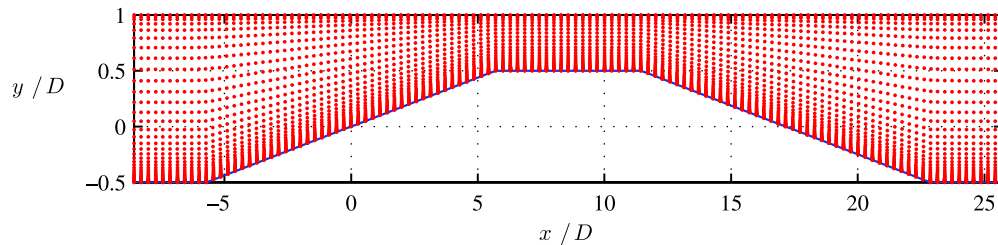
Figure 10. Example model grid for the case with $D/k_N = 10^3$, $a/k_N = 5 \times 10^3$, $a/D = 5$, and $\beta = 5°$, using $N_x = 120$ and $N_y = 60$. All results are based at the location $x/D = 0$. The vertical scale on Figure 10 is grossly exaggerated.
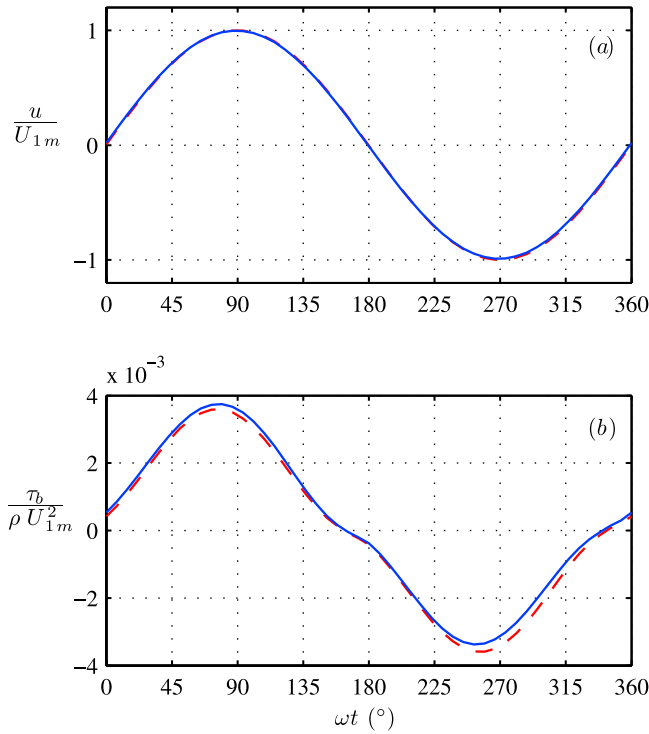
Figure 11. Computed time series of (a) free stream velocity and (b) bed shear stress for the converging-diverging case (full lines) with slope angle $\beta = 5°$, roughness $a/k_N = 2 \times 10^3$, and depth $D/k_N = 10^3$ (i.e., $a/D = 2$, $sa/D = 0.175$), with $Re = 5 \times 10^6$. The dashed lines are from an otherwise identical simulation on a flat bed, i.e., with $\beta = 0°$.

$D = 0$. Hence, if we relate these simulations to waves propagating normal to a beach, positive bed shear stresses can be considered as directed onshore.

[31] The model will be used to systematically assess differences in both peak and mean bed shear stresses induced by a sloping bottom, in the convergent and divergent half cycles. We consider a parametric study where the following dimensionless variables are systematically varied:

$$\frac{a}{k_N}, \qquad \frac{D}{k_N}, \qquad \text{and} \qquad \beta. \qquad (24)$$

Note that a particular choice of the first two quantities likewise defines an additional dimensionless variable

$$\frac{a}{D} = \frac{a/k_N}{D/k_N}, \qquad (25)$$

which plays an important role, as will be discussed later in section 5. Within the numerical model two bottom slopes will be considered, corresponding to $\beta = 2°$ and $5°$ (i.e., $s \approx 0.0349$ and 0.0875, respectively), along with the two values $D/k_N = 10^2$ and 10^3. For a given combination of these parameters, the nondimensional roughness a/k_N is then varied over a suitable range. All simulations use a large Reynolds number, fixed at $Re = 5 \times 10^6$.

[32] Note that to minimize undesired effects created from the flat-slope transitions within the model domain, the total free stream orbital length must be less than that of the sloping section, i.e., we must strictly require $2a < L_s$. This can be shown to be equivalently

$$\frac{a}{D} < \frac{1}{2s}. \qquad (26)$$

This constraint formally requires, for example, that $a/D < 14.4$ for $\beta = 2°$, and $a/D < 5.7$ for $\beta = 5°$. To consider as wide a range as possible, we will therefore restrict results with $\beta = 2°$ to $a/D \leq 10$, and with $\beta = 5°$ to $a/D \leq 5$.

4.2. Results

[33] As an example, a computed free stream velocity and corresponding bed shear stress time series from a case with $a/k_N = 2 \times 10^3$, $D/k_N = 10^3$ (i.e., $a/D = 2$), and $\beta = 5°$ are presented in Figure 11. Also shown on Figure 11 for comparison are results from an otherwise identical simulation on a flat bed (dashed lines). While the free stream velocities do not differ too significantly, it is seen that the bed slope induces skewness in the bed shear stress time series, resulting in an increased peak and reduced trough relative to the flat bed result. The effects observed in this rough-turbulent case are qualitatively similar to those observed previously in hydraulically smooth circumstances (see again, e.g., Figures 4b and 4c). This should be expected, as the underlying driving mechanisms are the same for both rough and smooth cases.

[34] Results for the bed shear stresses will now be presented in the form of friction factor diagrams, for the full range of parameters tested. For this purpose we define separately a friction factor for the convergent

$$f_c = \frac{2\tau_{bm}}{\rho U_{1m}^2} \qquad (27)$$

and divergent

$$f_d = -\frac{2\tau_{b,\min}}{\rho U_{1m}^2} \qquad (28)$$

half periods, where τ_{bm} and $\tau_{b,\min}$ are, respectively, the maximum and minimum bed shear stresses occurring over a cycle. These are both analogous to the standard wave friction factor defined by (16). We also define similar quantities in terms of the time-averaged bed shear stresses over the two half periods:

$$\bar{f}_c = \frac{2\bar{\tau}_{bc}}{\rho U_{1m}^2}, \qquad (29)$$

$$\bar{f}_d = -\frac{2\bar{\tau}_{bd}}{\rho U_{1m}^2}, \qquad (30)$$

where $\bar{\tau}_{bc}$ and $\bar{\tau}_{bd}$ respectively represent bed shear stresses averaged over the converging and diverging half periods. Notice that as the bed slope (or alternatively, the ratio a/D) tends to zero, we must expect that $f_c = f_d = f_w$ and $\bar{f}_c = \bar{f}_d$,
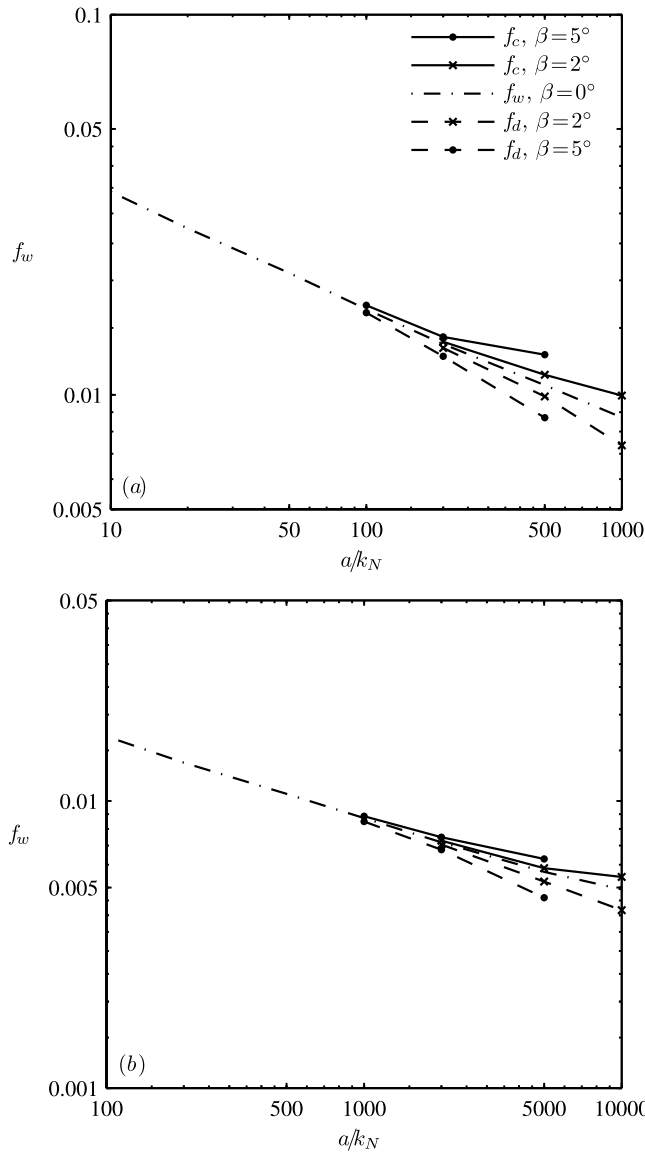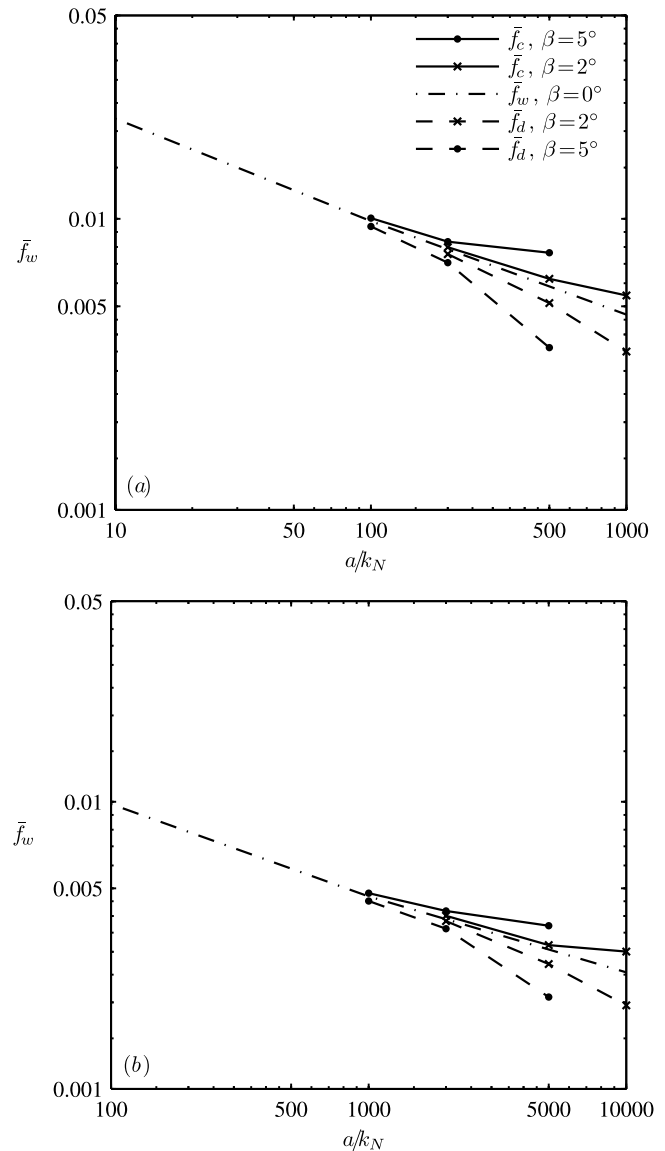
Figure 12. Computed wave friction factor f_c, f_w, and f_d versus nondimensional roughness a/k_N for various slope angle β with (a) $D/k_N = 10^2$ and (b) $D/k_N = 10^3$.

i.e., the results will converge to those on a flat bed when the slope becomes small and/or the tunnel becomes very deep, since large depths reduce the induced pressure gradient for a given slope.

[35] Friction factor diagrams based on the maximum bed shear stresses in the converging and diverging directions are shown in Figures 12a (for fixed $D/k_N = 10^2$) and 12b (for $D/k_N = 10^3$). Also shown on Figures 12a and 12b are the model friction factors from simulations on flat beds, shown previously in Figure 1b. From Figures 12a and 12b we observe that, for a fixed D/k_N and slope angle β, the results do indeed converge to those from a similar flat bottom simulation as a/k_N (and hence a/D) is reduced, consistent with expectations. As a/k_N (likewise a/D) is increased, however, the maximum (absolute values of) bed shear stresses in the convergent and divergent half periods become noticeably different. For the slopes tested, which

represent realistic values for moderate to steep beaches, it is seen that the differences become pronounced for $a/k_N \geq D/k_N$ (i.e., for $a/D \geq 1$). Hence, these effects play a potentially important role for waves with sufficiently large a/D values (on appreciably sloping beds), potentially corresponding to conditions just outside the surf zone, as will be discussed later in section 6. Assessing the importance of these effects for wind waves, relative to those from other effects driving cross-shore sediment transport, e.g., from wave shape variations, is again the focus of Part 2.

[36] Similar data for the friction factors based on the time-averaged bed shear stresses in the convergent and divergent half periods are also presented in Figure 13. The same trends as discussed above are also evident on Figure 13. We hope these various friction factor diagrams will be useful for practical purposes, as the friction factor is commonly used in making bed shear stress predictions under wave motions.

Figure 13. Computed wave friction factor f_c, f_w, and f_d versus nondimensional roughness a/k_N for various slope angle β with (a) $D/k_N = 10^2$ and (b) $D/k_N = 10^3$.

[37] We finally mention that *Justesen* [1988] previously developed a simpler one-equation turbulence model, based in part on mixing length theory, for the numerical simulation of oscillatory flow on a sloping bed. Diagrams made using this simpler approach are reasonably similar to those based on the two-equation turbulence model presented here.

5. Similarity to Real Waves

[38] It now seems relevant to clarify precisely how the boundary layer in such a convergent-divergent oscillatory flow (as considered in this work) may be related to the boundary layer beneath real life waves in shoaling waters, as this has not previously been made clear. Obviously, such a setup gives an incomplete description: First, it should be stressed that because the imposed horizontal velocity profiles above the boundary layer are essentially uniform, the results should be considered most relevant for shallow water waves, where the tunnel depth D can be regarded as similar to the water depth h. Second, as the model does not have a free surface, horizontal variations from the progressive wave motion itself are neglected entirely. This in turn means that the vertical velocities from the progressive wave motion, as well as the corresponding streaming effects induced from this progressive motion are not included. Third, as turbulence in the model is generated exclusively from the wall regions, effects from externally generated turbulence (e.g., from the free surface beneath breaking waves) are obviously not included, and the results should only be considered quantitatively relevant outside the surf zone. Conveniently, this type of setup may therefore be thought of as isolating those effects induced from the bottom slope alone (i.e., effects from the other factors mentioned above would be in addition to those demonstrated here). From the point of view of the boundary layer, these bottom slope effects will be seen as spatial gradients in the amplitude of the free stream orbital motion a, which can be readily worked out. For the present purposes we will restrict attention to the first spatial gradient in a, with the aim of establishing the leading-order similarity condition for relating the oscillatory boundary layer at a particular location in a convergent-divergent tunnel to that beneath shoaling shallow-water waves.

[39] For the purposes of the present analysis, consider a sinusoidally varying flux

$$q = q_{1m}\sin(\omega t), \tag{31}$$

in a tunnel with local depth D and slope s, at a particular location $x = 0$. Assuming the boundary layer thickness is small relative to the tunnel depth D, the horizontal free stream velocity may then be approximated as

$$u = \frac{q}{D - sx} = U_{1m}\sin(\omega t), \tag{32}$$

where a Taylor series expansion yields

$$U_{1m} = \frac{q_{1m}}{D}\left(1 + \frac{xs}{D}\right) + O\left(\frac{s^2 x^2}{D^2}\right). \tag{33}$$

Truncating at the first two terms shown, the corresponding amplitude of the orbital motion (valid for small sx/D) is

$$a = \frac{U_{1m}}{\omega} = \frac{q_{1m}}{D\omega}\left(1 + \frac{xs}{D}\right), \tag{34}$$

with x-derivative at the point of interest

$$\left.\frac{da}{dx}\right|_{x=0} = \frac{q_{1m}s}{D^2\omega} = \frac{sa}{D}, \tag{35}$$

since $a|_{x=0} = q_{1m}/(D\omega)$. Notice that in a convergent-divergent tunnel, gradients in a are due entirely to the tunnel slope, and these are clearly governed by the nondimensional parameter sa/D, which was mentioned previously with regards to Table 1. Note that this parameter has already been previously identified by *Justesen* [1988, equation (6.80)], though it was not related to real waves in shoaling waters.

[40] When real waves propagate on a sloping beach, however, there will be a contribution to the gradient of a not only from the beach slope, but also from the process of shoaling, which modifies the wave height H and wave number k in space. For simplicity, we will restrict specific attention to linear shallow-water waves propagating normal to a beach, for which the energy flux per unit width reads

$$E_f = \frac{1}{8}g\rho\sqrt{gh}H^2 = \frac{1}{2}\rho\omega^2 a^2 h\sqrt{gh}, \tag{36}$$

where the amplitude of orbital bottom motion a is related to the wave height H via

$$a = \frac{H}{2kh}, \tag{37}$$

and the dispersion relation is

$$\frac{\omega}{k} = \sqrt{gh}. \tag{38}$$

Assuming a mild beach slope, conservation of energy flux may be assumed, which implies $dE_f/dx = 0$. Neglecting constants in (36), this leads to
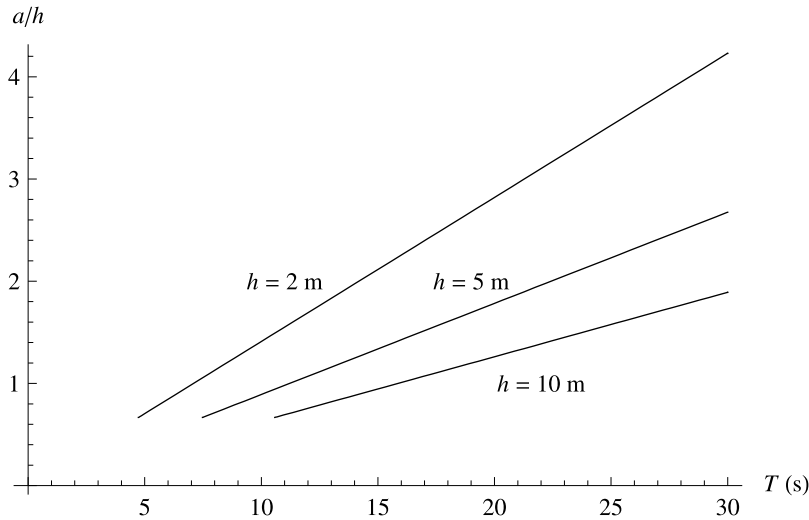
$$\frac{d}{dx}\left(a^2 h^{3/2}\right) = 2ah^{3/2}\frac{da}{dx} + \frac{3}{2}a^2 h^{1/2}\frac{dh}{dx} = 0. \tag{39}$$

Taking the local beach slope to be $S = -dh/dx$ and solving for da/dx we obtain

$$\frac{da}{dx} = \frac{3}{4}\frac{Sa}{h} = \frac{3}{8}\frac{H}{h}\frac{S}{kh}. \tag{40}$$

Hence, by equating (40) and (35) we arrive at the similarity condition to relate oscillatory flow at a particular location within a convergent-divergent tunnel to linear (shallow-water) waves in shoaling water

$$\frac{sa}{D} = \frac{3}{4}\frac{Sa}{h}. \tag{41}$$

Figure 14. An estimation of the largest attainable values for a/h (made by fixing $H/h = 0.8$) for short-period waves ($T \leq 30$ s) at three water depths: $h = 2$ m, $h = 5$ m, and $h = 10$ m.

Unsurprisingly, we arrive at two parameters with a very similar form, with the tunnel slope s behaving similarly to the beach slope S, and tunnel depth D behaving similarly to the water depth h. A 3/4 factor must be used in relating these nondimensional quantities, however, to account for shallow-water shoaling effects, which create additional modifications to the gradients in a. We stress that, because this condition only matches the first-order spatial gradients in the amplitude a (i.e., higher-order gradients are neglected), the similarity is a local one, i.e., it can be used to relate the boundary layer effects from a point in a convergent-divergent tunnel to a particular location beneath shallow-water shoaling waves. It does not, however, imply that the similarity will hold for the full length of the respective sloping sections (essentially, the established similarity will break down as sx/D becomes large).

[41] When discussing the applicability of their original experiments involving oscillatory motion in a convergent-divergent tunnel *Sumer et al.* [1993] concluded that their experiments did not reproduce shoaling effects in real waves. If D is taken to be the actual water depth h, and the tunnel slope s is strictly taken as representing the actual beach slope S, as supposed in their discussion, then this is a correct line of reasoning. However, this section demonstrates that, from the point of view of the boundary layer, shoaling effects may in fact be conceptually incorporated within oscillatory converging-diverging flow by modifying the physical interpretation of the tunnel slope s to locally account for both bottom slope and shoaling effects, as suggested by (41). We hope this discussion will be useful in interpreting any future (as well as past) numerical/physical experiments involving oscillatory flow in a convergent-divergent section.

6. Geophysical Relevance

[42] Finally, in order to more easily relate the previously presented results to waves in a natural setting, it seems relevant to more directly address their geophysical relevance. This can conveniently be done by considering the range of the parameter a/h which will likely be encountered in practice under various wave settings, which can be considered similar to the parameter a/D in our various numerical simulations. On the basis of linear shallow-water theory we may invoke (37) and (38) to arrive at the explicit relation

$$\frac{a}{h} = \frac{H}{2kh^2} = \frac{HT}{4\pi h}\sqrt{\frac{g}{h}}. \tag{42}$$

To obtain a leading-order estimate for the upper bounds of a/h likely to be reached in practice (for wind waves outside the surf zone), we will fix the wave height to water depth ratio to be large $H/h = 0.8$, which is a commonly used breaking threshold. Resulting curves for a/h versus wave period $T \leq 30$ s are then provided in Figure 14 for three depths: $h = 2$ m, 5 m, and 10 m, which have been chosen to be represent a realistic range of incipient breaking depths ranging from calm to storm conditions. From Figure 14 we can see, for example, that prior to waves breaking at a depth $h \approx 5$ m (felt to be typical of moderate storm conditions) values within the range $1 \leq a/h \leq 2$ are likely to be reached, for waves having periods of say $10 \text{ s} \leq T \leq 20$ s, a typical range for wind waves or swell. Alternatively, slightly larger values, up to say $a/h \approx 3$ might be reached under more calm conditions, as indicated by the $h = 2$ m curve. Thus, for wind waves near breaking, it seems likely that $a/h = O(1)$ would often be reached, which from Figures 12 and 13 is around the threshold where the induced bed slope effects become important for realistic beach slopes. It is also important to emphasize that in many physical situations $a/h = O(1)$ would not be locally attained, for example, at locations where the waves are not steep (i.e., far outside the surf zone) or, for example, where the period is much shorter than say $T = 5$ s. In these circumstances, the converging-diverging effects discussed herein would be expected to play a minor role in the boundary layer dynamics for realistic beach slopes.

[43] Many of the results presented herein, however, have considered larger values of $a/D = O(10)$. In particular, the

modeled experiments of *Sumer et al.* [1993] used $a/D = 20–30$, as indicated in Table 1. (The reason for the large experimental values is due in part to the physical constraints of the experimental facility, as discussed previously by *Sumer et al.* [1993].) On the basis of the analysis above, values of a/h this high would seem unlikely to be reached under typical conditions involving wind waves outside the surf zone. While the experiments of *Sumer et al.* [1993] have primarily been used as model validation in the present work, it turns out that they too would seem to have geophysical relevance for waves having longer timescales, e.g., those arising from earthquake-generated tsunamis. For example, a typical earthquake-generated tsunami might have a period $T = 15$ min, with a wave height $H = 1$ m in the deep ocean, where the water depth is say $h = 4$ km. On the basis of linear shallow-water theory, i.e., conservation of (36), such a wave would shoal (neglecting three-dimensional effects as a first approximation) to a wave height $H = 3.8$ m at a depth $h = 20$ m, locally yielding $a/h = 9.4 = O(10)$. Larger values for a/h can easily be envisioned by manipulating the input values, or by continuing the shoaling for the present example to shallower water depths, though this example seemingly provides a sufficient order-of-magnitude indication.

[44] Thus, given the large range of timescales possible for water waves, all of the results considered herein would seem to have potential geophysical relevance. In Part 2, however, we will restrict the focus to conditions reasonably representative of the wind wave regime. Largely on the basis of the analysis above, in Part 2 the range $1 \leq a/D \leq 2$ will therefore be considered in more detail, combined with bottom slopes $0 \leq s \leq 0.10$, in order to assess the likely importance (or lack thereof) of the discussed bed slope effects on bed shear stress quantities and boundary layer streaming, relative to those from a number of other factors affecting cross-shore boundary layer dynamics.

7. Conclusions

[45] This work has utilized a numerical model solving Reynolds-averaged Navier-Stokes equations, combined with a two-equation k-ω model for turbulence closure, to consider the converging-diverging effects induced by bottom slope on turbulent wave boundary layers. The model has first been validated via flat bed friction factor diagrams for both hydraulically smooth and rough beds, demonstrating acceptable accuracy for wave orbital amplitude to roughness ratios of say $a/k_N \geq 20$. Additionally, the model has been validated for streaming beneath a skewed free stream velocity signal, and finally against experimental data from *Sumer et al.* [1993] for bed shear stresses and streaming induced within oscillatory flow in a smooth converging-diverging tunnel. Both the experiments and model results predict period-averaged bed shear stresses and near-bed streaming in the converging direction, a direct result of modifications to pressure gradients induced by the bottom slope. A conceptually useful explanation for the streaming in these circumstances is also provided, by relating the near-bed flow in converging and diverging half periods to that in steady converging and diverging (diffuser) flows. The comparisons herein mark the first numerical modeling of the experimental work of *Sumer et al.* [1993].

[46] The numerical model has been subsequently used to perform a parametric study for similar cases involving oscillatory converging-diverging flow on hydraulically rough beds, the regime most likely encountered in practice. Important nondimensional quantities have been identified and varied systematically over realistic ranges. The results have been presented in the form of friction factor diagrams, based on both peak and mean bed shear stresses within converging and diverging half cycles. The results demonstrate significant differences between the two half periods for moderate to large bottom slopes combined with large values of the orbital length to depth ratio, i.e., $a/D \geq 1$. This can arise in practice, for example, when shallow water waves are near breaking, and these effects may therefore make significant contributions to cross-shore sediment transport under certain circumstances.

[47] Finally, by equating the induced gradients in the free stream orbital lengths, we have derived a similarity condition for relating oscillatory boundary layer flow at a particular location in a converging-diverging tunnel to that beneath real (shallow-water) waves in shoaling waters. This clarifies the physical interpretation of past, as well as possible future, experiments involving oscillatory flow in a convergent-divergent tunnel, which would be typical of those performed in experimental u-tube facilities. The geophysical relevance of the various results has also been discussed, indicating that the results with $a/D = O(1)$ are likely relevant for wind waves as they approach breaking, whereas results with $a/D = O(10)$ would be more relevant for longer wave, e.g., those having periods more typical of ocean tsunamis.

[48] This work is the first of two parts, the second of which (herein referred to as Part 2) will assess the importance of the converging-diverging effects from bed slope studied here on bed shear stress parameters and streaming, relative to those from other factors important within cross-shore boundary layer dynamics (e.g., wave skewness, wave asymmetry, conventional steady streaming, and combined wave-current effects).

References

Bagnold, R. A. (1946), Motion of waves in shallow water. Interaction between waves and sand bottoms, *Proc. R. Soc. London, Ser. A*, *187*, 1–15.

Bijker, E. W., J. P. T. Kalkwijk, and T. Pieter (1974), Mass transport in gravity waves on a sloping bottom, in *Proceedings of the 14th International Conference on Coastal Engineering*, pp. 447–465, Am. Soc. of Civ. Eng., Reston, Va.

Blondeaux, P. (1987), Turbulent boundary layer at the bottom of gravity waves, *J. Hydraul. Res.*, *25*, 447–463.

Blondeaux, P., M. Brocchini, and G. Vittori (2002), Sea waves and mass transport on a sloping beach, *Proc. R. Soc. London, Ser. A*, *458*, 2053–2082.

Chu, V. H., and C. C. Mei (1970), On slowly-varying Stokes waves, *J. Fluid Mech.*, *41*, 873–887.

Davies, A. G., and Z. Li (1997), Modelling sediment transport beneath regular symmetrical and asymmetrical waves above a plane bed, *Cont. Shelf Res.*, *17*, 555–582.

Dixen, M., F. Hatipoglu, B. M. Sumer, and J. Fredsøe (2008), Wave boundary layer over a stone-covered bed, *Coastal Eng.*, *55*, 1–20.

Fredsøe, J., and R. Deigaard (1992), *Mechanics of Coastal Sediment Transport*, World Sci., Singapore.

Fuhrman, D. R., J. Fredsøe, and B. M. Sumer (2009), Bed slope effects on turbulent wave boundary layers: 2. Comparison with skewness, asymmetry, combined wave-current, and streaming effects, *J. Geophys. Res.*, *114*, C03025, doi:10.1029/2008JC005053.

Gonzalez-Rodriguez, D., and O. S. Madsen (2007), Seabed shear stress and bedload transport due to asymmetric and skewed waves, *Coastal Eng.*, *54*, 914–929.

Hassan, W. N., and J. S. Ribberink (2005), Transport processes of uniform and mixed sands in oscillatory sheet flow, *Coastal Eng.*, *52*, 745–770.

Hedegaard, I. B. (1985), Wave generated ripples and resulting sediment transport in waves, *Ser. Pap. 36*, Inst. of Hydrodyn. and Hydraulic Eng., Tech. Univ. of Den., Kongens Lyngby, Denmark.

Hino, M., M. Kashiwayanagi, A. Nakayama, and T. Hara (1983), Experiments on the turbulence statistics and the structure of a reciprocating oscillatory flow, *J. Fluid Mech.*, *131*, 363–400.

Holmedal, L. E., and D. Myrhaug (2006), Boundary layer flow and net sediment transport beneath asymmetrical waves, *Cont. Shelf Res.*, *26*, 252–268.

Hsu, T.-J., and D. M. Hanes (2004), Effects of wave shape on sheet flow sediment transport, *J. Geophys. Res.*, *109*, C05025, doi:10.1029/2003JC002075.

Jakobsen, N. G. (2007), Shape and dimension of ripples, M.S. thesis, Tech. Univ. of Den., Kongens Lyngby, Denmark.

Jensen, B. L., B. M. Sumer, and J. Fredsøe (1989), Turbulent oscillatory boundary layers at high Reynolds numbers, *J. Fluid Mech.*, *206*, 265–297.

Jensen, J. H., and J. Fredsøe (2001), Sediment transport and backfilling of trenches in oscillatory flow, *J. Waterw. Port Coastal Ocean Eng.*, *127*, 272–281.

Jensen, J. H., E. Ø. Madsen, and J. Fredsøe (1999a), Oblique flow over dredged channels. I: Flow description, *J. Hydraul. Eng.*, *125*, 1181–1189.

Jensen, J. H., E. Ø. Madsen, and J. Fredsøe (1999b), Oblique flow over dredged channels. II: Sediment transport and morphology, *J. Hydraul. Eng.*, *125*, 1190–1198.

Jonsson, I. G., and N. A. Carlsen (1976), Experimental and theoretical investigations in an oscillatory turbulent boundary layer, *J. Hydraul. Res.*, *14*, 45–60.

Justesen, P. (1988), Turbulent wave boundary layers, Ph.D. thesis, Inst. of Hydrodyn. and Hydraulic Eng., Tech. Univ. of Den., Kongens Lyngby, Denmark.

Kamphuis, J. W. (1975), Friction factor under oscillatory waves, *J. Waterw. Port Coastal Ocean Eng. Div. Am. Soc. Civ. Eng.*, *101*, 135–144.

Longuet-Higgins, M. S. (1953), Mass transport in water waves, *Philos. Trans. R. Soc. London, Ser. A*, *245*, 535–581.

Lundgren, H., and I. G. Jonsson (1961), Bed shear stress induced by a wave motion, *Basic Res. Prog. Rep. 1*, pp. 3–5, Coastal Eng. Lab., Tech. Univ. of Den., Kongens Lyngby, Denmark.

Patel, V. C., and J. Y. Yoon (1995), Application of turbulence models to separated flow over rough surfaces, *J. Fluids Eng.*, *117*, 235–241.

Puleo, J. A., O. Mouraenko, and D. M. Hanes (2004), One-dimensional wave bottom boundary layer model comparison: Specific eddy viscosity and turbulence closure models, *J. Waterw. Port Coastal Ocean Eng.*, *130*, 322–325.

Ribberink, J. S., and A. A. Al-Salem (1994), Sediment transport in oscillatory boundary layers in cases of rippled beds and sheet flow, *J. Geophys. Res.*, *99*, 12,707–12,727.

Ribberink, J. S., and A. A. Al-Salem (1995), Sheet flow and suspension of sand in oscillatory boundary layers, *Coastal Eng.*, *25*, 205–225.

Sleath, J. F. A. (1987), Turbulent oscillatory flow over rough beds, *J. Fluid Mech.*, *182*, 369–409.

Sumer, B. M., B. L. Jensen, and J. Fredsøe (1987), Turbulence in oscilatory boundary layers, in *Advances in Turbulence*, edited by C. Comte-Bellot and J. Mathieu, pp. 556–567, Springer, Berlin.

Sumer, B. M., T. S. Laursen, and J. Fredsøe (1993), Wave boundary layer in a convergent tunnel, *Coastal Eng.*, *20*, 317–342.

Tjerry, S. (1995), Morphological calculation of dunes in alluvial rivers, Ph.D. thesis, Inst. of Hydrodyn. and Hydraulic Eng., Tech. Univ. of Den., Kongens Lyngby, Denmark.

Tjerry, S., and J. Fredsøe (2005), Calculation of dune morphology, *J. Geophys. Res.*, *110*, F04013, doi:10.1029/2004JF000171.

Wilcox, D. C. (1994), Turbulence modeling in CFD, 1st ed., report, DCW Ind., Inc., La Canada, Calif.

Zou, Q., and A. E. Hay (2003), The vertical structure of the wave bottom boundary layer over a sloping bed: Theory and field measurements, *J. Phys. Oceanogr.*, *33*, 1380–1400.

Zou, Q., A. E. Hay, and A. J. Bowen (2003), Vertical structure of surface gravity waves propagating over a sloping seabed: Theory and field measurements, *J. Geophys. Res.*, *108*(C8), 3265, doi:10.1029/2002JC001432.

―――――――――――――――

J. Fredsøe, D. R. Fuhrman, and B. M. Sumer, Department of Mechanical Engineering, Technical University of Denmark, DK-2800 Kgs. Lyngby, Denmark. (jf@mek.dtu.dk; drf@mek.dtu.dk; bms@mek.dtu.dk)